Effect of chromium substitution on structural, magnetic and magnetocaloric properties of GdFe12–Cr intermetallic compounds, Mössbauer spectrometry and ab initio calculations

M. Saidi, S. Walha, E.K. Hlil, Lotfi Bessais, M. Jemmali

Version of Record: https://www.sciencedirect.com/science/article/pii/S0022459621000645
Manuscript_6fcc7665d8bf1aca6c0598063cede5ff

Effect of chromium substitution on structural, magnetic and magnetocaloric properties of $GdFe_{12-x}Cr_x$ intermetallic compounds, Mössbauer spectrometry and ab initio calculations

M. Saidi,[1,2] S. Walha,[2] E. K. Hlil,[3] L. Bessais * [a],[1] and M. Jemmali[2,4]

[1] *Univ Paris Est Creteil, CNRS, ICMPE, UMR 7182, 2 rue Henri Dunant, F-94320 Thiais, France*

[2] *University of Sfax, Faculty of Science, LSME, BP1171-3018 Sfax, Tunisia.*

[3] *Univ. Grenoble Alpes, CNRS, Grenoble INP, Institut Néel, 38000 Grenoble, France*

[4] *Department of Chemistry, College of Science and Arts, Ar-rass, Qassim University, PO Box 53, Buraydah Postcode 51921, Saudi Arabia.*

(Dated: January 24, 2021)

[a] Corresponding author ; electronic mail: bessais@icmpe.cnrs.fr

Abstract

The single-phase intermetallic compounds $GdFe_{12-x}Cr_x$ (x = 2, 2.5 and 3), elaborated by arc-melting method and annealed at 1073 K, crystallize in the $ThMn_{12}$-type structure with the $I4/mmm$ space group. The structural, magnetic and magnetocaloric properties of these intermetallic compounds were studied extensively by means of X-ray powder diffraction (XRD), Mössbauer spectrometry and magnetic measurements. The Rietveld analysis of X-ray diffraction patterns reveals that the lattice parameters of $GdFe_{12-x}Cr_x$ (x = 2, 2.5 and 3) compounds increase linearly with increasing Cr content up to $x = 3$, and proves that Cr atom prefers $8i$ sites in the $ThMn_{12}$ structure and that Fe occupies $8i$, $8f$ and $8j$. The Mössbauer spectra study based on the Wigner-Seitz cell volumes correlation with the isomer shift parameter of each specific site $8i$, $8f$ and $8j$, confirms the preferred inequivalent crystallographic site of Cr atoms. *Ab initio* calculations of $GdFe_{12-x}Cr_x$ were performed using the density functional theory (DFT) based on the full potential linearized augmented plane wave (FLAPW). The calculated data are in good agreement with the results of the magnetic measurements as well as with the Mössbauer spectrometry. The variation of magnetization (M) vs. temperature (T) reveals that all compounds exhibit a second-order ferromagnetic to paramagnetic phase transition in the vicinity of the Curie temperature (T_C). The substitution of Fe by Cr yields enhancement of the magnetic ordering transition temperature. The maximum magnetic entropy change (ΔS_M) was estimated from isothermal magnetization curves and it increases from 1.82 J/kg.K for x = 2, to 2.95 J/kg.K for x = 3, under a field change of 1.5 T. The relative cooling power (RCP) is in the range of 12.5 J/kg for x = 2 and 30.4 J/kg for x = 3. Our results suggest that such substituted compounds could be considered as a potential candidate for magnetic refrigeration technology

PACS numbers: 75.50.Bb, 75.50.Tt, 76.80.+y

Keywords: Intermetallic compounds; Magnetic materials; Magnetocaloric effect; DFT; Electronic structure ; Mössbauer spectrometry.

I. INTRODUCTION

Refrigeration occupies an important place in both domestic and industrial areas; it is used in various applications such as agri-food and medical preservation which operate with a huge amount of refrigeration requirements [1]. Conventional gas compression-expansion refriger-

ators presents a danger to the environment, due to the use of toxic and environmentally detrimental refrigerants such as hydro chlorofluorocarbons (HCFCs), chlorofluorocarbons (CFCs) and ammonia (NH_3) [2, 3] which could escape into the environment causing the depletion of the ozone layer and enhancing the greenhouse effect. Thus, from an environmental conservation perspective, research on future refrigeration technologies is more and more oriented toward other techniques, such as room temperature magnetic refrigeration.

In addition, magnetic refrigerators are much more compactly built thanks to the magnetic materials used as a refrigeration media. In this context, magnetic cooling technology based on magnetocaloric effect (MCE) was considered as a potential mean for a novel solid cooling technology with high energy-efficiency, ecological cleanliness and environmental friendliness [4–9].

During the past few years, scientists investigated the study of the intermetallic compounds based on rare-earth (R) and transition-metal (T) because of their various magnetic and magnetocaloric properties thanks to their crystal structures and their constituent elements, which allow potential industrial applications in different fields [10–26].

The properties displayed by these intermetallic compounds give rise to a great variety of functional materials for technological applications such as high performance permanent magnets, high density magnetic recording and specially magnetic refrigeration [10–13, 15–40]. Furthermore, interest in these intermetallic compounds is due to the intrinsic properties of the high magnetic moment per atom and the strong magnetocrystalline anisotropy provided by the localized $4f$-rare earth element, and the high magnetic coupling strength of the moments of the itinerant $3d$-transition metal element [41, 42]. Among this attractive class of compounds, iron-rare earth intermetallic compounds (RFe) display a great variety of crystalline structures and different magnetic behaviors depending on the stoichiometry and the nature of the R atom [13, 43].

The $R\mathrm{Fe}_{12}$ intermetallic compounds with the tetragonal ThMn_{12}-type crystal structure were recognized as promising hard magnetic materials since the 1980´ s [12, 44, 45]. However, due to thermodynamically unstable nature of the the binary $R\mathrm{Fe}_{12}$ compounds, their synthesis becomes impossible for the entire series of rare-earth elements. To solve this, it was found that the small substitution of a stabilizing $3d$-transition metal such as (M= Si, Ti, V, Cr, Nb, Mo and W [11, 46–49] for Fe in the $R\mathrm{Fe}_{12}$ compound resulted in the formation of the $R(\mathrm{Fe},M)_{12}$ compounds. The properties of ternary rare earth iron-rich compounds of

the type $R\mathrm{Fe}_{12-x}M_x$ (R = Y, Nd, Sm, Gd, Tb, Dy, Ho, Er, Tm and Lu with M = Si, Ti, V, Cr, Mo and W) have been studied intensively [50–53]. The tetragonal $R\mathrm{Fe}_{12-x}M_x$ ferromagnetic compounds have been particularly investigated due to their fairly high values of Curie temperature, saturation magnetization, and high magnetocrystalline anisotropy [11, 54, 55], which opens possibilities for applications as permanent magnet materials [56–59].

Recently, we have constructed the Gd-Fe-Cr ternary phase diagram at 1073 K [60] in order to explore new ternary compounds and develop Fe rich materials at low cost and with good magnetic and magnetocaloric properties. Both SEM-EDS and X-ray diffraction analysis proved the existence of the $\mathrm{GdFe}_{12-x}\mathrm{Cr}_x$ new ternary solid solution for the first time, which extended from about 15.4 at. % Cr to 23.1 at. % Cr at 1073 K.

In the current research, we have focused our attention on the study of the magnetic properties, as well as the magnetocaloric effects of the $\mathrm{GdFe}_{12-x}\mathrm{Cr}_x$ compounds. Those studies have been stimulated for a great deal by the possibility of using these materials for magnetic refrigeration application. So far, no investigation of the magnetocaloric proprieties of these compounds have ever been made. Moreover, the Mössbauer spectroscopy have been used to accurately localize the Cr substitution site and to determine the microscopic magnetic properties of the three inequivalent crystallographic Fe sites. In addition, we calculated the electronic properties of $\mathrm{GdFe}_{12-x}\mathrm{Cr}_x$ using Density-Functional theory (DFT) to determine the theoretical magnetic moments and hyperfine fields in order to compare them with the experimental results.

II. CALCULATION METHOD

The purpose of the first-principles density functional theory (DFT) calculations is to determine the total energy, the total and the local magnetic moments as well as the hyperfine fields of the intermetallic $\mathrm{GdFe}_{12-x}\mathrm{Cr}_x$ compounds. The calculations are performed employing the full potential linearized augmented plane wave (FP-LAPW) method to solve the Kohn-Sham equations [61] of the density functional theory [62]. These calculations were carried out using the WIEN2k code [63, 64]. The generalized gradient approximation with the full Perdew-Burke-Ernzerhof correlation energy (GGA-PBE) was used [65].

We have selected for the expansion of the wave functions the cut-off parameter as follows $R_{\mathrm{MT}} \times K_{\max} = 7$, with $K_{\max}$ being the magnitude of the largest $\vec{K}$ vector. In the interstitial

region [66], the Fourier expansion of potential and charge energy were chosen with $G_{\max} = 12\,\mathrm{Ry}^{\frac{1}{2}}$. The number of 1200 k-points were used in the Brillouin zone.

The used muffin-tin radius R_{MT} is equal to 2.50, 2.14, and 2.12 Bohr, for Gd, Fe, and Cr atoms, respectively. In order to separate the valence and core states, we have chosen the cut-off energy $E = -7\,\mathrm{Ry}$. As the total energy difference is smaller than $10^{-4}\,\mathrm{Ry}$ and the charge is less than 10^{-4} electron charges, we assume that the system is stable and the convergence of self-consistent-field cycle will be reached.

The calculations of the hyperfine fields for $GdFe_{12-x}Cr_x$ compounds are conducted using the self-consistent approach of Blügel *et al.* [67, 68] that includes the relativistic generalizations of the dipolar, contact, and orbital contributions to the hyperfine fields.

III. EXPERIMENTAL

In this paper, Gadolinium (99.99 wt.%), Iron (99.99 wt.%) and Chromium (99.99 wt.%) were used as starting elements for the experiment. Bulk buttons of the $ThMn_{12}$-type structure with the general formula $GdFe_{12-x}Cr_x$ ($x = 2, 2.5$ and 3), each weighing 0.5 g, were produced by arc-melting the elemental components under argon atmosphere in a water-cooled copper hearth using a non-consumable tungsten electrode. During the melting process, a pure zirconium button was used to get rid of oxygen. To ensure a high degree of homogeneity, the ingots were turned over and re-melted several times. All the samples were weighed before and after melting to ensure that no significant mass loss occurred. The weight losses were generally less than 1%. After melting, all the samples were wrapped in tantalum foil and sealed under vacuum in silica tubes. In order to improve the atomic diffusion kinetics, ensure a good crystallinity, and minimize the amount of other possible impurities, treatments using heat were performed in a resistance furnace at 1073 K during seven days. After this thermal treatment, the samples were quickly quenched in cold water. In order to prepare powders for the different measurements, the arc-melted buttons alloys were ground by means of an agate mortar.

To determine the crystallographic structure and identify the phase purity, an X-ray powder diffraction investigation was performed through the use of a Bruker D8 diffractometer (Bruker AXS, Karlsruhe, Germany) with an automatic divergence slit (CuKα radiation λ = 1.540562 Å). The X-ray diffraction data were obtained in a scan step size of 0.015° and

a counting time of 13.5 s per point, over a 2θ range from 20° to 80°. The X-ray diffraction patterns of the $ThMn_{12}$-type structure was refined by Rietveld analysis [69, 70] using the Fullprof software [71, 72]. The peak-shape function was selected as Thompson-Cox-Hastings pseudo-Voigt type [73, 74]. To measure the quality of refinement, the "goodness-of-fit" indicators χ^2 and R_B (Bragg factor) from the program output are set as follows:

$$R_B = 100\frac{\sum_K |I_K(o) - I_K(c)|}{\sum_K I_K(o)} \quad \text{and} \quad \chi^2 = \frac{\sum_i w_i |y_i(o) - y_i(c)|^2}{N - P}$$

where $I_K(o)$ is the observed Bragg intensity and $I_K(c)$ is the calculated one. $y_i(o)$ is the intensity observed at the i^{th} step in the step scanned powder diffraction pattern, $y_i(c)$ is that calculated, and w_i is the weight of the observation. N is the total number of points used in the refinement and P the number of refined parameters.

The magnetic properties of the compounds were experimentally studied using a DSM-8 MANICS differential sample Magneto Susceptometer. The magnetic transition temperatures in the studied compounds $GdFe_{12-x}Cr_x$ ($x = 2, 2.5$ and 3) were found with temperature-dependent magnetization measurements $M(T)$ under an applied field of 0.12 T and a heating rate of 5 K/min. The Curie temperature was identified from the minimum of the temperature derivative of the magnetization dM/dT vs temperature. The change of magnetic entropy was identified using the temperature and the change of applied magnetic field through numerical integration of the isothermally measured $M(H)$ curves.

To identify the iron-containing phases [20, 21, 75], we used the ^{57}Fe Mössbauer spectra, which were obtained on a constant-acceleration spectrometer. The γ-radiation is emitted from the radioactive parent isotope, ^{57}Co, which decays to the excited state of the ^{57}Fe Mössbauer isotope. The transmitted intensity of this radiation through an absorber containing ^{57}Fe atoms is calculated as a function of the X-ray energy that is varied through Doppler shifting the source relative to the absorber. This explains the reason why the energy scale is calculated in mm/s and energies are measured in mm/s by Mössbauer spectrometry. The Mössbauer absorbers (which were 25 mg/cm^2 thick) were prepared from powdered compounds. The ^{57}Fe Mössbauer spectra were obtained using 25 mCi ^{57}Co in Rh matrix γ-ray source, in transmission geometry. The spectrometer was calibrated using a specimen of $\alpha-$Fe that shows a line-width of 0.25 mm/s for . The estimated errors of the fitted spectra

are: $\pm\,0.01$ mm/s for isomer shift δ and quadrupole interaction 2ε, and $\pm\,0.1$ T for hyperfine fields $\mu_0 H$.

IV. RESULTS AND DISCUSSION

A. Structure analysis

It is noteworthy that RT_5 ($CaCu_5$-type) and RT_{12} ($ThMn_{12}$-type) structures have a close connection. Their stability depends mainly on geometric considerations. The tetragonal $I4/mmm$ structure is obtained from the hexagonal $P6/mmm$ structure [52]. Therefore, when two dumbbell pairs ($T-T$) substitute for $2R$ atoms over a $4RT_5$-type cell, the $ThMn_{12}$-type phase is as follows:

$$\mathbf{4\ (RT_5)\ -\ 2R\ +\ 4T\ (dumbbell)\ =\ 2\ (RT_{12})}$$

The lattice parameters of the tetragonal $ThMn_{12}$-type phase can be turned into those of hexagonal $CaCu_5$-type phase through the following equations:

$$\mathbf{c(1/12)\ =\ a(1/5)}$$

$$\mathbf{c(1/5)\ =\ a(1/12)/2}$$

A schematic representation of the tetragonal $ThMn_{12}$-type crystal structure of the $GdFe_{10}Cr_2$ intermetallic compound is illustrated in Figure 1. The rare-earth atoms are found in the corners and centers of the tetragonal prisms in the single $2a$ crystallographic site. On the other hand, the transition elements are scattered over the three inequivalent sites which are $8i$, $8j$, and $8f$. The iron atoms fully occupy the $8j$ and $8f$ sites while the $8i$ site is occupied by a blend of iron and chromium atoms. In Figure 1, the Gd atoms which occupy the site $2a$ (0, 0, 0) are represented by large orange spheres. Furthermore, the three different Wyckoff sites $8i$ (x, 0, 0), $8j$ $(x, 0, \frac{1}{2})$ and $8f$ $(\frac{1}{4}, \frac{1}{4}, \frac{1}{4})$, populated by Fe1/Cr, Fe2 and Fe3 atoms, are illustarted by medium spheres in green, pink and yellow respectively.

The X-ray diffraction patterns of $GdFe_{12-x}Cr_x$ ($x = 2, 2.5$ and 3) compounds are plotted in Figure 2. The data were refined by the Rietveld refinement technique [70] through the use of the Fullprof program [71, 72]. The Rietveld fitting demonstrate a good harmony between the observed and calculated profiles for all the sample compounds. The X-ray diffraction

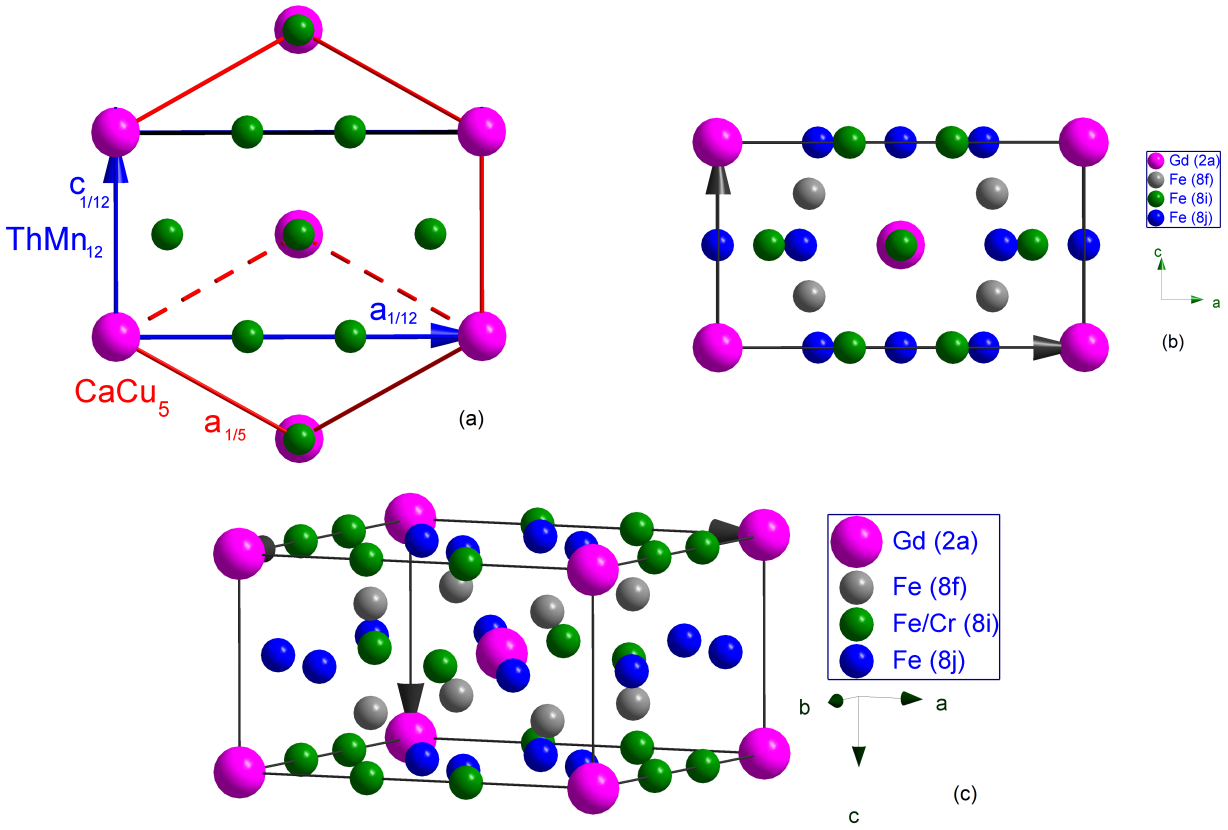

FIG. 1. Schematic representation of the relationship between $CaCu_5$ (along [001] axis) and $ThMn_{12}$ (along [010] axis) structures (a), illustration of atomic arrangements in $GdFe_{10}Cr_2$ crystal structure along [010] axis (b), and the tetragonal $I4/mmm$ crystal structure of $GdFe_{10}Cr_2$ (c).

patterns of the $GdFe_{12-x}Cr_x$ ($x = 2, 2.5$ and 3) compounds, annealed at 1073 K, are indexed in the tetragonal $ThMn_{12}$-type structure with $I4/mmm$ space group. The Rietveld analysis reveals that the polycrystalline compounds are single phase. The results of the representative refinement such as the crystallographic unit cell parameter values along with the reliability factors χ^2 and R_B acquired from the best refinement are illustrated in Table I. The iron atomic positions for the different chromium content values x) of $GdFe_{12-x}Cr_x$ compounds are also listed in this Table I.

The Rietveld refinement proves that the substitution of iron by chromium increase the unit cell parameters a and c, for the $GdFe_{12-x}Cr_x$ ($x = 2, 2.5$ and 3) compounds. Keeping in mind that the chromium atomic radius ($r = 1.66$ Å) is larger than that of the iron ($r = 1.56$ Å), one would expect this enhancement of crystallographic parameters. In Figure 3, we present the variation of the unit cell parameters a and c of the 1:12 phase as a function of

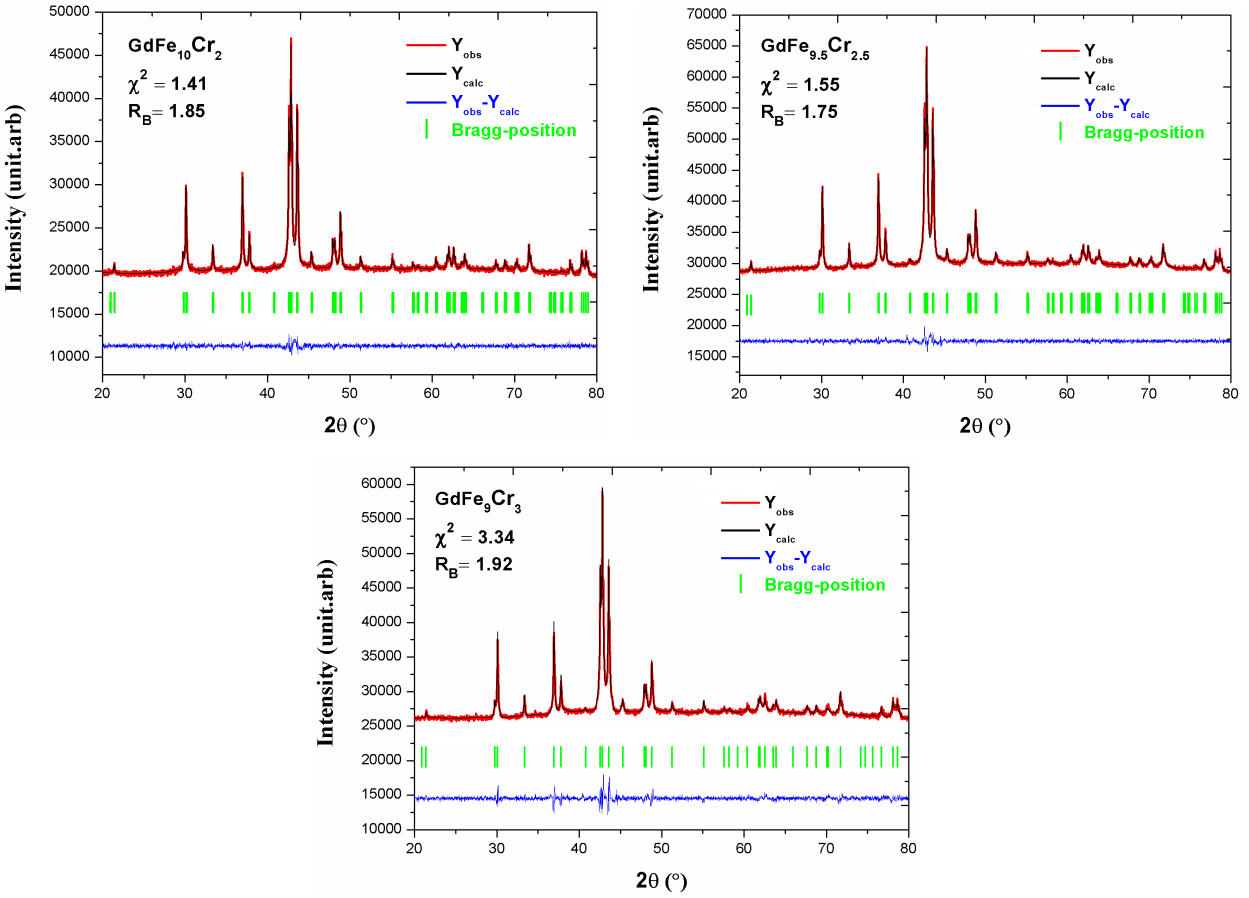

FIG. 2. Rietveld refinement of XRD patterns of the $GdFe_{12-x}Cr_x$ (x = 2, 2.5 and 3) compounds.

TABLE I. XRD analysis results obtained by Rietveld method on the $GdFe_{12-x}Cr_x$ (x = 2, 2.5 and 3) compounds.

	$x = 2$	$x = 2.5$	$x = 3$
a (Å)	8.480(6)	8.485(1)	8.487(8)
c (Å)	4.755(3)	4.756(7)	4.757(3)
V (Å^3)	342.018(4)	342.471(2)	342.737(3)
χ^2	1.41	1.55	3.34
R_B	1.85	1.75	1.92
$x\{8j\}$	0.2727	0.2733	0.2771
$x\{8i\}$	0.3624	0.3625	0.3645

x Cr content in the $GdFe_{12-x}Cr_x$ ($x = 2, 2.5$ and 3) compounds. The atomic positions are

not affected by the substitution of iron by chromium.

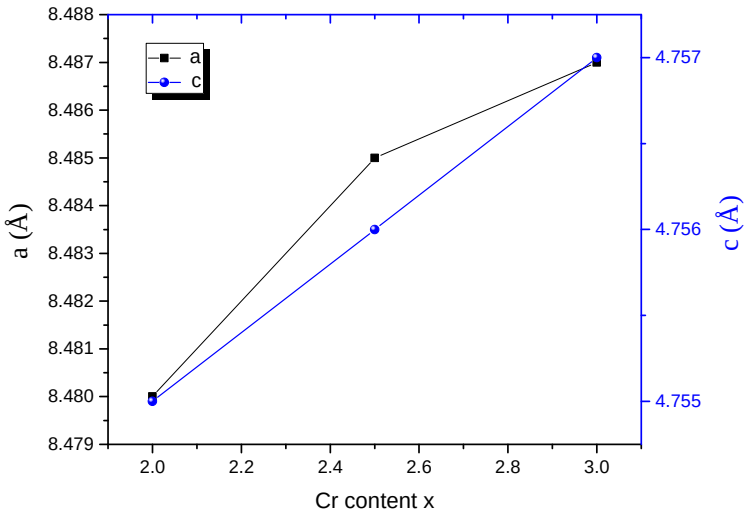

FIG. 3. Variation of $GdFe_{12-x}Cr_x$ ($x = 2, 2.5$ and 3) a and c vs. x content.

Let's remind that for the $SmFe_{12-x}Mo_x$ ($x = 1, 1.5$ and 2) compounds, S. Khazzan *et al.* [76] reported that the partial substitution of iron by molybdenum resulted in a small variation of the lattice parameters showing therefore a slight increase of the cell volume. In addition, W. X. Zhong *et al.* [77] and D. P. Middleton *et al.* [78], showed that the unit cell parameters a and c for the $GdFe_{12-x}Al_x$ ($x = 4, 56, 8$ and 10) and $GdFe_{12-x}Mo_x$ ($x = 1.5$ and 3) compounds increase when increasing Al and Mo content x, respectively. As the Fe has a smaller atomic radius than Al and Mo, this evolution of crystallographic parameters is expected.

In this study, Rietveld analysis was also used to investigate the preferential substitution site. In a first step, the refinement was performed with Cr randomly distributed among all the crystallographic sites $8i$, $8j$, and $8f$. In a second step, the distribution of Cr was done for the three sites separately. The best agreement factor R_B of the $GdFe_{12-x}Cr_x$ compounds were obtained with Cr atoms located in $8i$ site and Fe atoms occupying $8i$, $8j$, and $8f$ sites. In order to verify and confirm this outcome, we have carried out the Mössbauer spectrometry measurement as a complementary method.

It is worthy to note that, J. J. Bara *et al.* [79] have deduced from the numerical analysis of Mössbauer spectra that in the $RFe_{10}Cr_2$ (R= Y, Nd, Gd, Tb, Dy, Ho, Er and Tm) intermetallic compounds, Cr tends to avoid the sites $8j$ and $8f$ while preferentially occupying the site $8i$. Moreover, Ohashi *et al.* used the Rietveld refinement to find the site preference

in $SmFe_{10}Cr_2$, and concluded that Cr was preferentially located at $8i$ site [54]. This finding is in agreement with our result. Likewise, the $SmFe_{12-x}Mo_x$ and $YFe_{12-x}Mo_x$ systems were studied by S. Khazzan *et al.* [76] and Hu *et al.* [80]. They showed that Mo atoms did not exhibit any preference for $8j$ and $8f$ sites, and there are pronounced preferences for $8i$ site. On the other hand, the large transition metal atoms (M = Ti, V, Nb, Mo, Ta, W) occupy the $8i$ site of $R(Fe,M)_{12}$ because this site is characterized by the largest Wigner-Seitz cell volume. However, Al and Si atoms, which allow for two direct bonds with the rare-earth atoms, strongly prefer the $8f$ sites [13, 81].

B. Hyperfine parameters

The Mössbauer spectrometry approach appears as the efficient tool to confirm the Cr location obtained by Rietveld refinement and to understand the effect of the Cr substitution in iron-rich systems for our $GdFe_{12-x}Cr_x$ (x =2, 2.5 and 3) compounds. Three types of nuclear interactions are measured: magnetic hyperfine H_{HF}, isomer shift δ and quadrupole splitting 2ε.

The isomer shift increases due to the interaction between the s electrons and the nuclear charge density. The s electron density can be shielded by the electrons p and d which reduce this density. The isomer shift decreases when the electron density s increases. Increasing the d electron density results in more s electron shielding and hence increases δ.

The isomer shift decreases when the s electron density increases, the isomer shift decreases. However, the increase in the d electron density could cause a lower attraction of the s electron by the nuclear charge and consequently increases δ, as showed by the following equation:

$$\delta = Ze^2 \left(\psi(0)_a^2 - \psi(0)_s^2\right) \left(\frac{\Delta R}{R}\right) \times R^2$$

$\Delta R/R$ the nuclear factor and R is the effective nuclear radius, $\psi(0)_s^2$ the electron density at the source nucleus and $\psi(0)_a^2$ represents the electron density of the absorbent.

Figure 4 presents the room temperature Mössbauer spectra of the $GdFe_{12-x}Cr_x$ (x = 2, 2.5 and 3) compounds. It is important to note that the ferromagnetic sextets constituting the Mössbauer spectra result from the convolution of many sub-spectra. Consequently, a relevant physical model related to structural characteristics is needed to analyze such

spectra. The refinement of the observed hyperfine parameters for $GdFe_{12-x}Cr_x$ (x = 2, 2.5 and 3) compounds was based on the following conditions: (i) the abundance of the sextets subspectra are derived by a multinomial distribution law; (ii) the correlation between the Wigner-Seitz cell volume (WSCV) and the isomer shift (δ), the larger isomer shift, the larger the WSCV [82–85]; (iii) the correlation between the hyperfine field and the near-neighbor environments of the three inequivalent iron sites in the $ThMn_{12}$-type structure.

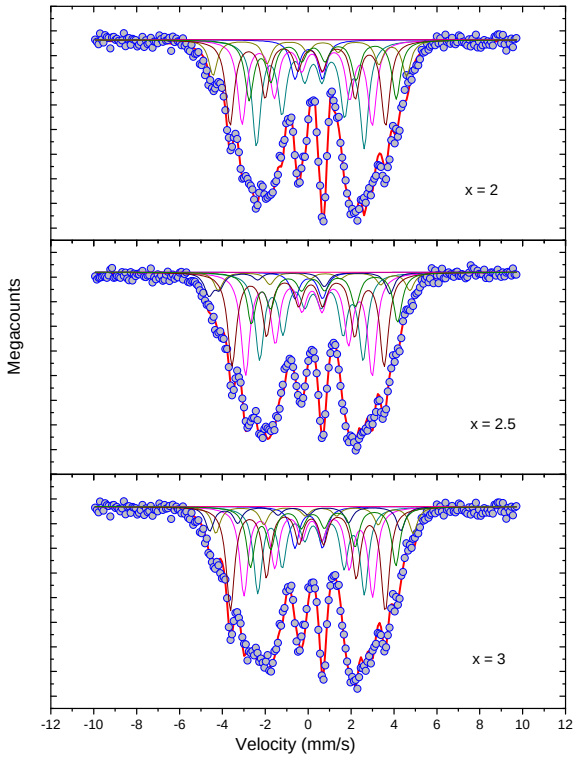

FIG. 4. Room temperature Mössbauer spectra of $GdFe_{12-x}Cr_x$. The blue circle symbol scatter plot and the red solid line are the experimental and calculated spectra, respectively.

The number of nearest-neighbor sites for $8f$ are (2, 4, 4), for $8i$ are (4, 5, 4) and for $8j$ are (4, 4, 3), where the numbers in parenthesis refer to $8f$, $8i$ and $8j$ site neighbors, respectively. The highest the number of iron nearest-neighbors, the highest the iron hyperfine field. The number of iron near neighbors for the tetragonal $I4/mmm$ structure type for $GdFe_{10}Cr_2$ compound are summarized in Table II.

We calculated the relative intensity of the different iron inequivalent crystallographic sites $8i$, $8j$ and $8f$ with a multinomial distribution as follows. For a given configuration $\ell = (n_1, \ldots, n_k)$ with k the number of neighbors in the site ℓ. K = 4, 2, 4 for $8i$, $8j$, and $8f$ site, respectively. As the atoms are randomly distributed on a certain site ℓ, the probability

TABLE II. Number of nearest neighbors nn of the iron sites in $GdFe_{10}Cr_2$.

Site	Fe$\{8i\}$	Fe$\{8j\}$	Fe$\{8f\}$
Fe$\{8i\}$	5	4	4
Fe$\{8j\}$	4	3	4
Fe$\{8f\}$	4	4	2

P_α is given by

$$P_\alpha = \frac{N!}{\prod_{k=0}^{K} n_k} \prod_{k=0}^{K} p_k^{n_k}$$

Where, P_α is the probability to find k Cr atoms in a shell of n $8i$, $8j$, $8f$ nearest neighbors, p_k is the relative atomic abundance of Cr atoms in different sublattices. $N = 4$ for $8i$, $N = 2$ for $8j$ and $N = 4$ for $8f$ site. We have neglected the subspectra with intensity lower than 1.5%.

The Wigner-Seitz Cell volume have been calculated for each crystallographic atomic site with the radius values of 1.88 Å for Gd, 1.26 Å for Fe and 1.39 Å for Cr. The resulting WSCV from such calculations lead to the following volume sequence: $8i > 8j > 8f$. The calculated WSCV are indicated in Table III. This sequence of WSCV could explain the fact that Cr atoms, with a larger radius than iron, have a preference for the $8i$ site. This result is in agreement with the previous study using Mössbauer spectrometry of $SmFe_{11}Ti$ [86].

Furthermore, the results of the refined Mössbauer spectra, demonstrate that the hyperfine fields are following this sequence $H_{HF}\{8i\} > H_{HF}\{8j\} > H_{HF}\{8f\}$ which is in line with the number of Fe nearest neighbors of each site (Fig. 5). Moreover, the classification obtained for the isomer shift is $\delta\{8i\} > \delta\{8j\} > \delta\{8f\}$. This classification matches closely the Wigner-Seitz cell volume sequence. As an example, the Mössbauer hyperfine parameters and WSCV for $GdFe_{10}Cr_2$ are summarized in Table III.

We have found that the average Fe magnetic moment $\langle\mu_{Fe}\rangle$ is equal to 1.96, 1.89 and 1.85 μ_B for $x = 2$, $x = 2.5$ and $x = 3$, respectively. For this calculation, we have used a conversion factor of $12.8\,T/\mu_B$ which was found by J. J. Bara *et al.* from the refinement of the Mössbauer spectra for $YFe_{10}Cr_2$ [79]. These results of magnetic moments will be compared

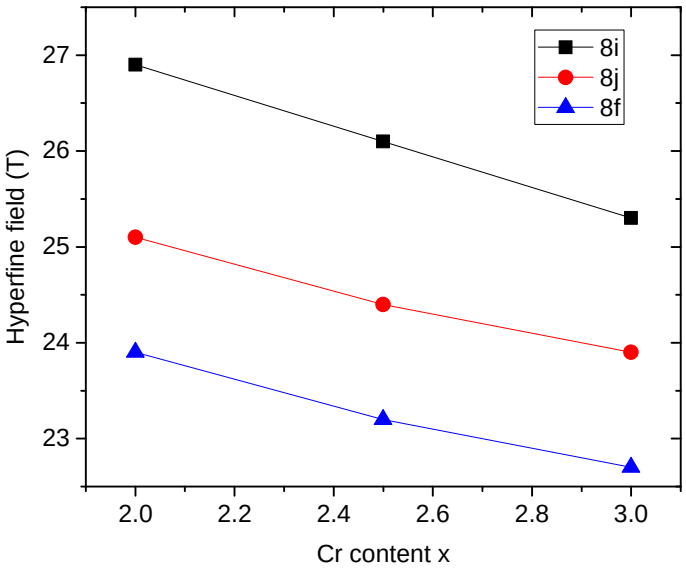

FIG. 5. Compositional dependence of the weighted average hyperfine fields for the three inequivalent crystallographic sites for $GdFe_{12-x}Cr_x$ (x = 2, 2.5 and 3) compounds.

TABLE III. Mössbauer hyperfine parameters for $GdFe_{10}Cr_2$: Hyperfine field H_{HF}(T), quadrupole interaction 2ε (mm/s), isomer shift δ (mm/s), and Wigner-Seitz Cell Volume WSCV (Å^3).

	Fe{8i}	Fe{8j}	Fe{8f}	wt.ave.
$\mu_0 H_{HF}$	26.9	25.1	23.9	25.1
δ	0.21	0.15	0.06	0.14
2ε	-0.01	0.05	0.28	0.11
WSCV	13.4	12.1	10.9	12.3

to those derived from the saturation magnetization measurements and those obtained by Density-functional theory calculations.

C. Magnetic properties

Following the structural and the Mössbauer analyzes, we investigated the magnetic properties of our samples. The Curie temperature is a consequence of exchange interaction in ferromagnetic compounds. The magnetization as a function of the temperature was measured in the range 450-650 K, under an applied field $\mu_0 H = 0.12$ T. The thermal variation

of magnetization of the $GdFe_{12-x}Cr_x$ (x= 2, 2.5 and 3) compounds annealed at 1073 K, is given in Figure 6.

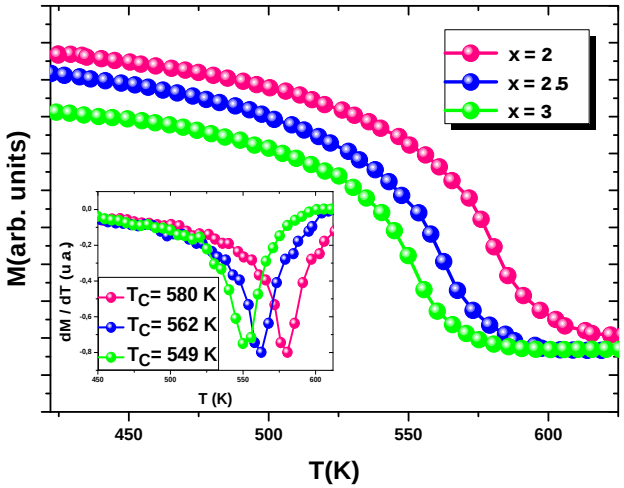

FIG. 6. Magnetization vs temperature for $GdFe_{12-x}Cr_x$ (x = 2, 2.5 and 3) compounds. Tne inset : dM/dT vs temperature..

The value of T_C was defined as the temperature at which dM/dT vs temperature exhibits a minimum as illustrated in the inset of Figure 6. According to the curves, all the compounds exhibit a clear magnetic transition from a ferromagnetic behavior for $T < T_C$ to a paramagnetic behavior for $T > T_C$. The Curie temperature of $GdFe_{10}Cr_2$ compound is found to be equal to 580 K, which is consistent with the results published in Ref [87]. Obviously, the increase of Cr content does not affect the ferromagnetic behavior, but rather causes a gradual reduction in Curie temperature, from 580 K for x = 2, to 549 K for x = 3. This decrease of T_C can be interpreted in terms of the magnetic dilution occurring with the substitution of magnetic Fe with non-magnetic Cr. Figure 7 presents the evolution of T_C vs. Cr content for different $GdFe_{12-x}Cr_x$ composition.

Moreover, M_S was derived from the fit of the $M(H)$ plot at room temperature using the well known saturation approach law [88]:

$$M = M_S\left(1 - \frac{b}{H^2}\right)$$

with

$$b = \left(\frac{8}{105}\right)\left(\frac{K}{M_S}\right)^2$$

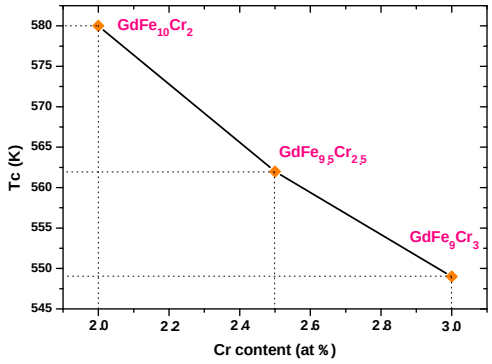

FIG. 7. Curie temperature vs Cr content for $GdFe_{12-x}Cr_x$ (x = 2, 2.5 and 3) compounds.

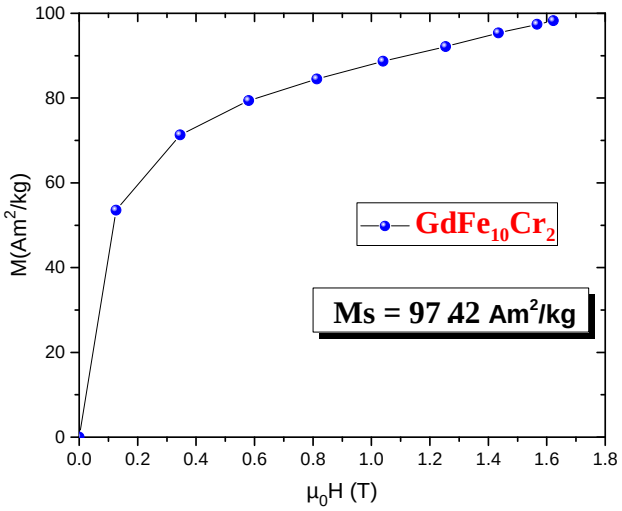

FIG. 8. $M(H)$ curve for $GdFe_{9.5}Cr_{2.5}$ at T = 300 K.

where K and M_s are respectively anisotropy constant and saturation magnetization. As an example, Figure 8 shows $M(H)$ for $GdFe_{9.5}Cr_{2.5}$ at T = 300 K. For this compound we found M_S = 84.97 Am^2/kg. The anisotropy field can be easily deduced from $H_a = 2K/M_S$. The values of M_s, K and H_a are listed in Table IV.

M_S decreases with the substitution of Fe by Cr atoms as follows: 97.4 Am^2/kg (14.30 μ_B) for x = 2, 85.0 Am^2/kg (12.44 μ_B) for x = 2.5 and 78.2 Am^2/kg (11.42 μ_B) for x = 3.

The substitution of Fe by Cr in $GdFe_{12-x}Cr_x$ causes a decrease of magnetization which is a direct consequence of the modification of the exchange interactions. A. Kowakzyk and A. Wrzeciono have observed similar behavior in $R_2Fe_{14-x}Cr_xB$ compounds [89]. These results are in coherent with measured Mössbauer hyperfine fields. Indeed, taking a conversion factor

TABLE IV. Magnetic properties of $GdFe_{12-x}Cr_x$.

x	M_s(Am^2kg^{-1})	T_c(K)	K($MJ.m^{-3}$)	$\mu_0 H_a$(T)
2	97.4	580	1.51	3.3
2.5	85.0	565	1.37	3.1
3	78.2	549	1.35	2.9

of $12.8\,T/\mu_B$, we found a total magnetic moment of $14.1\,\mu_B$, $12.5\,\mu_B$ and $11.2\,\mu_B$ for $x = 2, 2.5$ and 3, respectively.

D. DFT calculations

To determine the Cr site in the $ThMn_{12}$ structure, we calculated the total energy of $GdFe_{10}Cr_2$ for the different crystallographic sites of substitution of the Fe atom by the Cr atom. We have found that the lowest energy corresponds to the substitution of Fe atoms in the $8i$ sites by Cr atoms (Table V). As a consequence, Cr atoms occupy preferentially the $8i$ site in $GdFe_{12-x}Cr_x$. Moze and Buschow also found that the chromium atom prefers to occupy the $8i$ site for $YFe_{12-x}Cr_x$ [90]. This result is consistent with both findings obtained by Rietveld refinement of the X-ray diagrams and the analysis of the Mössbauer spectra.

TABLE V. Calculated energy of $GdFe_{10}Cr_2$ with Cr atom occupying different sites.

Site	$8i$	$8j$	$8f$
E (Ry)	-104440.2439	-104440.2112	-104440.2025

In addition, the hyperfine fields were calculated for each crystallographic iron site $8i$, $8j$ and $8f$ (Table III). Having in mind that the experimental Mössbauer spectra are recorded at 300 K, the values of these experimental data derived from the refinement of the Mössbauer spectra are in reasonable agreement with the *ab initio* calculated hyperfine parameter (Table III).

The total spin-polarized densities of states of $GdFe_{12-x}Cr_x$ are calculated (Fig. 9). They show a typical metallic behavior in both spin-up and spin-down components. In order to compare the total density of states of bcc Fe (x12) with that of the hypothetical phases

TABLE VI. DFT calculated hyperfine fields $\mu_0 H_{\rm HF}$ (T) for $GdFe_{12-x}Cr_x$ ($x = 2, 2.5, 3$).

x	$8i$	$8j$	$8f$	$< \mu_0 H_{\rm HF} >$
2	28.5	27.2	25.6	26.9
2.5	28.0	26.3	25.1	26.1
3	27.4	25.8	24.5	25.3

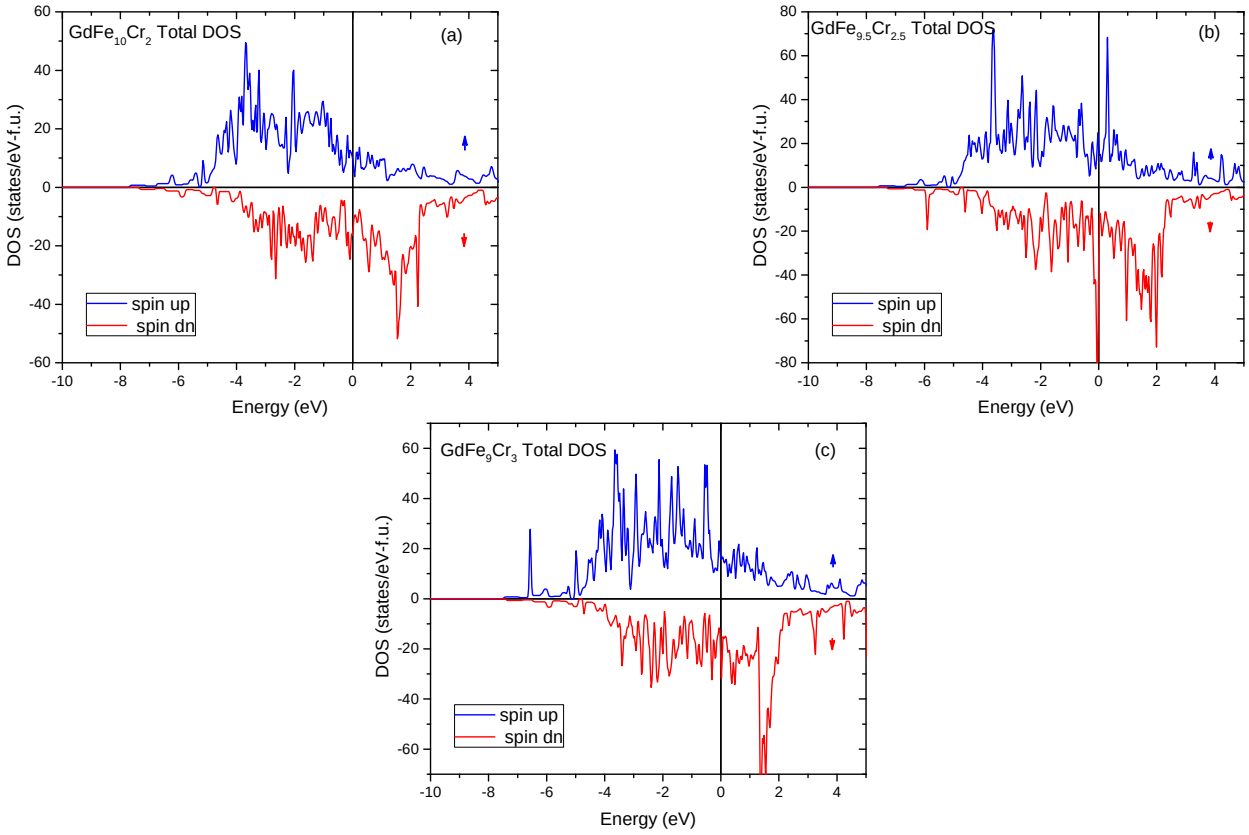

FIG. 9. Total density of states of $GdFe_{12-x}Cr_x$ for (a) $x = 2$, (b) $x = 2.5$ and (c) $x = 3$.

$GdFe_{12}$, we have plotted both results in Fig. 10. It is noteworthy that the DOS of $GdFe_{12}$ essentially corresponds to the contribution of the $3d$ bands, and that in the case of bcc Fe, for minority spin states, the valley separating the bonding and anti-bonding orbitals is deeper and wider than in the case of $GdFe_{12}$.

Fig. 11 shows the partial DOS of Fe $3d$ for the three crystallographic sites $8i$, $8j$ and $8f$ of $GdFe_{9.5}Cr_{2.5}$. The spin majority of those $3d$ states are mainly located between -5 eV and the Fermi Level, while the minority (spin-down) are distributed between -4 eV and the Fermi Level. We can see a relatively weak ferromagnetic state as the majority spin bands

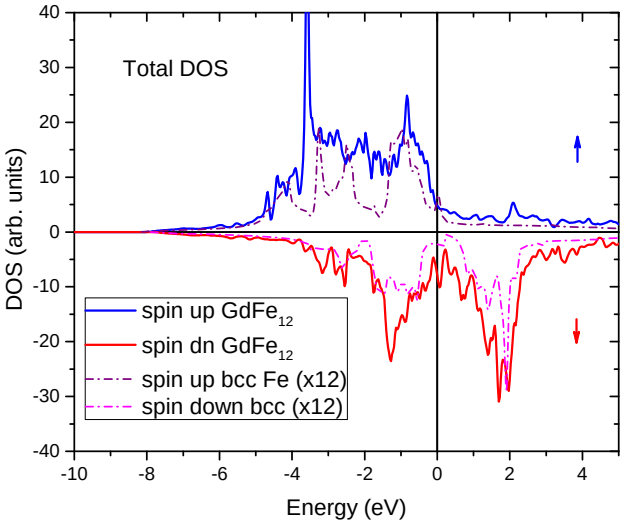

FIG. 10. Total density of states of $GdFe_{12}$ straight line and bcc Fe dashed line. The Fermi energy was taken as origin (black vertical line).

are not completely occupied, even so, the 8*i* local DOS gives the highest magnetic moment.

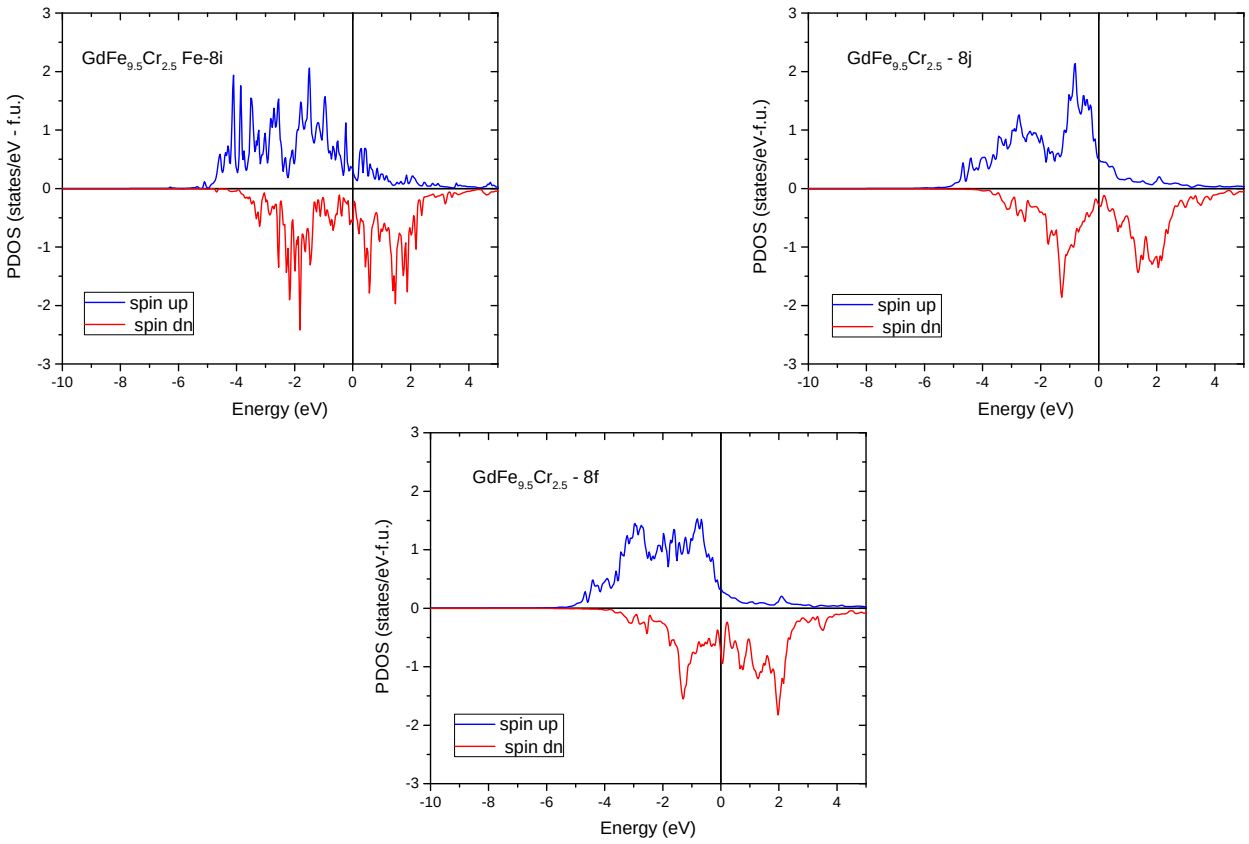

FIG. 11. Partial density of states for Fe-8*i*, Fe-8*j* and Fe-8*f* calculated for $GdFe_{9.5}Cr_{2.5}$. The origin of the energy is located at Fermi energy (black vertical line).

TABLE VII. Local calculated magnetic moments for the different crystallographic sites and the weighted average iron magnetic moment of $GdFe_{12-x}Cr_x$ ($x = 2, 2.5, 3$).

	Local calculated magnetic moment					$<\mu_{Fe}>$
x	Gd($2a$)	Fe($8i$)	Cr($8i$)	Fe($8j$)	Fe($8f$)	μ_B
2	6.85	2.46	-0.10	2.36	2.12	2.28
2.5	6.83	2.39	-0.13	2.24	1.87	2.11
3	6.82	2.31	-0.14	2.11	1.68	1.94

The iron moment is relatively low in the tetragonal $ThMn_{12}$ type-structure [15]. The average iron moment, calculated from the difference between the numbers of spin-up and spin-down, is $2.28\,\mu_B$ (for $GdFe_{10}Cr_2$), $2.11\,\mu_B$ (for $GdFe_{9.5}Cr_{2.5}$), and $1.94\,\mu_B$ (for $GdFe_9Cr_3$). The largest iron magnetic moment is $2.46\,\mu_B$ (for $GdFe_{10}Cr_2$), $2.39\,\mu_B$ (for $GdFe_{9.5}Cr_{2.5}$) and $2.31\,\mu_B$ (for $GdFe_9Cr_3$) for the $8i$ iron atom (Table VII). In Table VII the calculated local magnetic moments on the three inequivalent crystallographic sites as well as the weighted average magnetic moment are given. The magnetic moment follows the sequence $\mu_{Fe}\{8i\} > \mu_{Fe}\{8j\} > \mu_{Fe}\{8f\}$, which agrees with previous calculations and experiments [25, 52, 91–95]. This magnetic moment sequence follows the sequence $H_{HF}\{8i\} > H_{HF}\{8j\} > H_{HF}\{8f\}$ of the hyperfine fields obtained both by Mössbauer spectrometry, and by *ab initio* calculation.

We notice that the magnetic moment of the $8f$ Fe site is the smallest and could be a consequence of the short Fe-Fe distances of the nearest neighbors for those crystallographic sites. The presence of a single closest neighbor Gd atom at the $8i$ site, while at the other $8j$ and $8f$ sites, two Gd atoms are the closest neighbors, could be one of the reasons why the iron atoms have the highest magnetic moment value at the $8i$ site.

Moreover, Fig. 14 shows that the DOS around E_F is rather dominated by the $3d$ states mainly contributed by the Fe sub-networks. In addition, the $4f$ states of Gd are fully occupied (majority spins), while the $4f$ states of Gd with minority (negative) spins are empty and above the Fermi level. We can understand that by the fact that Gd $4f$ states couple in an anti-parallel fashion with the Fe $3d$ states. This result is in agreement with that found by Trygg *et al.* for $GdFe_{12}$ [96] and Liu *et al.* for $Gd(Co,Fe)_{12}B_6$ [97].

Overall, we have obtained a good agreement between the results of magnetic moments in μ_B/at. obtained from calculated hyperfine fields and electronic structure calculated by

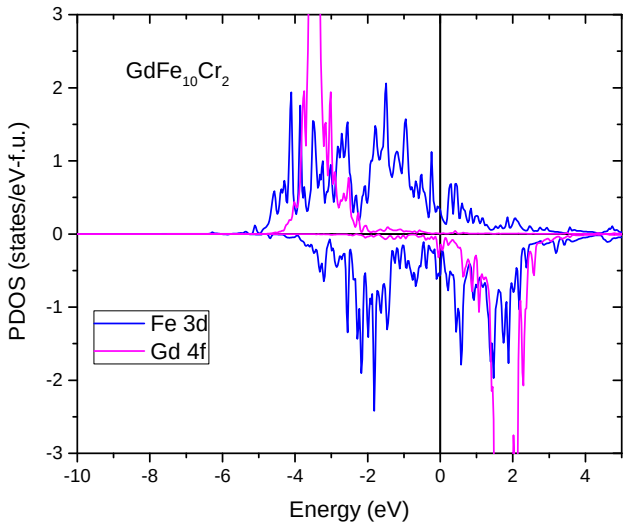

FIG. 12. Partial density of states of for Fe-3d and Gd-4f calculated for $GdFe_{10}Cr_2$.

DFT for $GdFe_{10-x}Cr_x$. Table VIII summarizes the comparison between experimental results deduced from Mössbauer Spectrometry and those obtained by theoretical calculations by DFT for $GdFe_{10}Cr_2$ as an example.

TABLE VIII. Comparison between the results of magnetic moments, in μ_B/at., obtained from calculated hyperfine fields and electronic structure calculated by DFT for $GdFe_{10}Cr_2$.

	Mössbauer	Calculated
$\langle\mu_{Fe}\rangle$	2.03	2.28
$\mu_{Fe}\{8i\}$	2.10	2.46
$\mu_{Fe}\{8j\}$	2.04	2.36
$\mu_{Fe}\{8f\}$	1.98	2.12

E. Magnetocaloric properties

The RFe$_{12}$-type compounds are suitable for permanent magnet application. However, in our study, we didn't focus our interest on this application because, we didn't optimize the microstructure of the studied compounds to obtain magnetically hard materials with high magnetic hysteresis. In this paper, we have investigated the magnetocaloric effect (MCE) of the $GdFe_{12-x}Cr_x$ ($x = 2, 2.5, 3$) compounds, because this effect has become very

important for cooling applications [98], due to the growing needs of refrigeration technology. Additionally, no investigation on the magnetocaloric proprieties of these compounds has been done so far. MCE is an intrinsic property of magnetic materials defined as the heating or the cooling of magnetic material (reversibly) due to the application or the removal of an external magnetic field, respectively, under adiabatic conditions. Such an effect is high when the magnetic compound is near T_C. The temperature (T) dependences of magnetization (M) under magnetic fields are studied in order to determine the nature of the magnetic transition, the variation of the magnetic entropy, and consequently the magnetocaloric effect.

Isothermal magnetization plots versus the applied magnetic field $M(\mu_0 H, T)$ of $GdFe_{12-x}Cr_x$ (x = 2, 2.5 and 3) compounds are measured at different temperatures with steps of 5 K under external magnetic fields. The resulting curves are shown in Figure 13. The isothermal curves exhibit a dependency between magnetization and the magnetic field applied at various temperatures. As we can see, at high temperatures well above the T_C value, the curves $M(\mu_0 H, T)$ clearly decrease with an almost linear behavior which is typical for paramagnetic materials. Moreover, below T_C the magnetizations rise rapidly under the low magnetic field, and then tend to saturate as the field value increases as a feature of ferromagnetic materials.

The so called Arrott plots were studied and successfully applied as a key tool to determine the nature of the feromagnetique-pramagnetique phase transition. Hence, to give a better understanding of the nature of the magnetic phase transition order, we present in Figure 14 the Arrott plots ($\mu_0 H/M$ vs. M^2) derived from the isotherms $M(\mu_0 H, T)$ for $GdFe_{12-x}Cr_x$ (x = 2, 2.5 and 3) compounds. As reported by Banerjee [99], an inspection of the sign of the slope of the straight line in the Arrott plots gives the nature of the magnetic phase transition order. In fact, the magnetic transition is of second order if the slope is positive and first order if negative. We can clearly see that in Figure 14, the curves ($\mu_0 H/M$ vs. M^2) exhibit a positive slope for all samples in the vicinity of T_C, which indicates that our samples undergo a second-order ferromagnetic-paramagnetic phase transition.

After having studied magnetic measurements of magnetization as a function of temperature $M(T)$ as well as magnetization as a function of the magnetic field at various temperatures $M(\mu_0 H, T)$, we have calculated $\Delta S(T)$ of all compounds. Based on the thermodynamic theory, magnetic entropy change is determined through the numerical integration of the magnetization isotherms, as shown by Maxwell's thermodynamic relation given by the

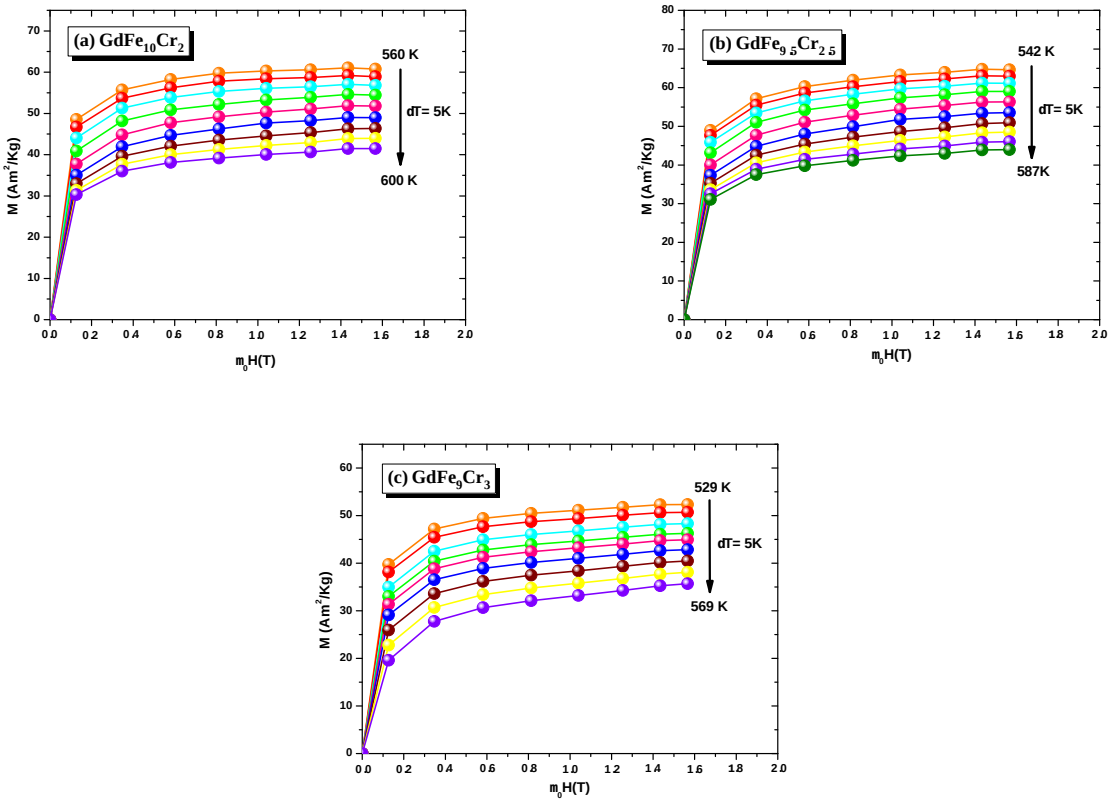

FIG. 13. Isotherm magnetization curves $M(H,T)$ of $GdFe_{12-x}Cr_x$ for (a) $x = 2$, (b) $x = 2.5$ and (c) $x = 3$.

following equation [100, 101]:

$$\Delta S = \mu_0 \int_0^H (\frac{\partial M}{\partial T}) dH$$

$$\Delta S(T_i, \Delta H) = \mu_0 \sum_j \frac{M_{i+1}(T_{i+1}, H_j) - M_i(T_i, H_j)}{T_{i+1} - T_i} \Delta H_j$$

Figure 15 shows $\Delta S_(T, \mu_0 H)$ for the $GdFe_{12-x}Cr_x$ ($x = 2$, 2.5 and 3) compounds. It can be clearly seen from this figure that the magnetic entropy change exhibits a sudden change around T_C. We can note that the curves soar to a maximum near T_C, indicating the ferromagnetic-paramagnetic transition with increasing temperature. Moreover, the peak value increases with increasing the value of the applied magnetic field. The maximum peak values of $\Delta S_{\max}$ for $x = 2$, $x = 2.5$ and $x = 3$ are equal to 0.92 J/kg K, 1.24 J/kg K and 1.56 J/kg K, respectively. Based on these results, we can deduce that $\Delta S_{\max}$ is found to increase with increasing Cr substitution in the $GdFe_{12-x}Cr_x$ ($x = 2$, 2.5 and 3) compounds. It's

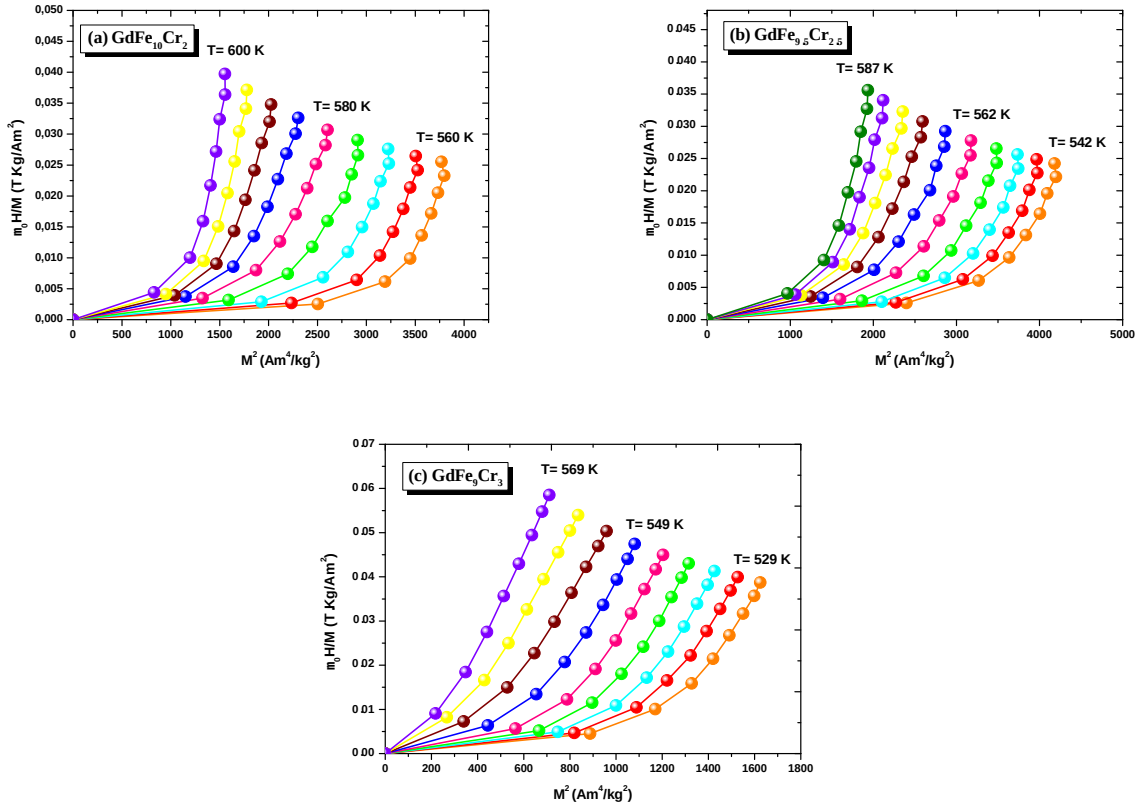

FIG. 14. The Arrott plots of $GdFe_{12-x}Cr_x$ for (a) $x = 2$, (b) $x = 2.5$ and (c) $x = 3$.

worthy to note that the $\Delta S_{\max}$ of these compounds are more significant than $SmNi_5$ ($\Delta S_{\max}$ = 1.2 J/kg K, $\mu_0 H = 1.5\ T$) [102] and $GdNi_3FeSi$ ($\Delta S_{\max} = 0.5$ J/kg K), $\mu_0 H = 1.5\ T$) [103].

It should be noted that $\Delta S_{\max}$ is not the only parameter determining an applicability of a material to magnetic refrigeration. The relative cooling power (RCP) is another important parameter of characterizing the magnetocaloric effect. In fact, the RCP parameter measures the amount of heat transferred between hot and cold sources in a magnetic refrigeration process. The defined parameter is a compromise between the width of the peak and the magnitude of $\Delta S_{\max}$. The relative cooling power expression is determined according to the following equation [82]:

$$RCP = -\Delta S_{\mathrm{Max}} \times \delta T_{FWHM}$$

Where $-\Delta S_{Max}$ is the maximum value of the entropy change (ΔS) and δT_{FWHM} is the full width half maximum of $\Delta S(T)$.

The obtained values of magnetic entropy change $-\Delta S_{\max}$, RCP and T_C for $GdFe_{12-x}Cr_x$

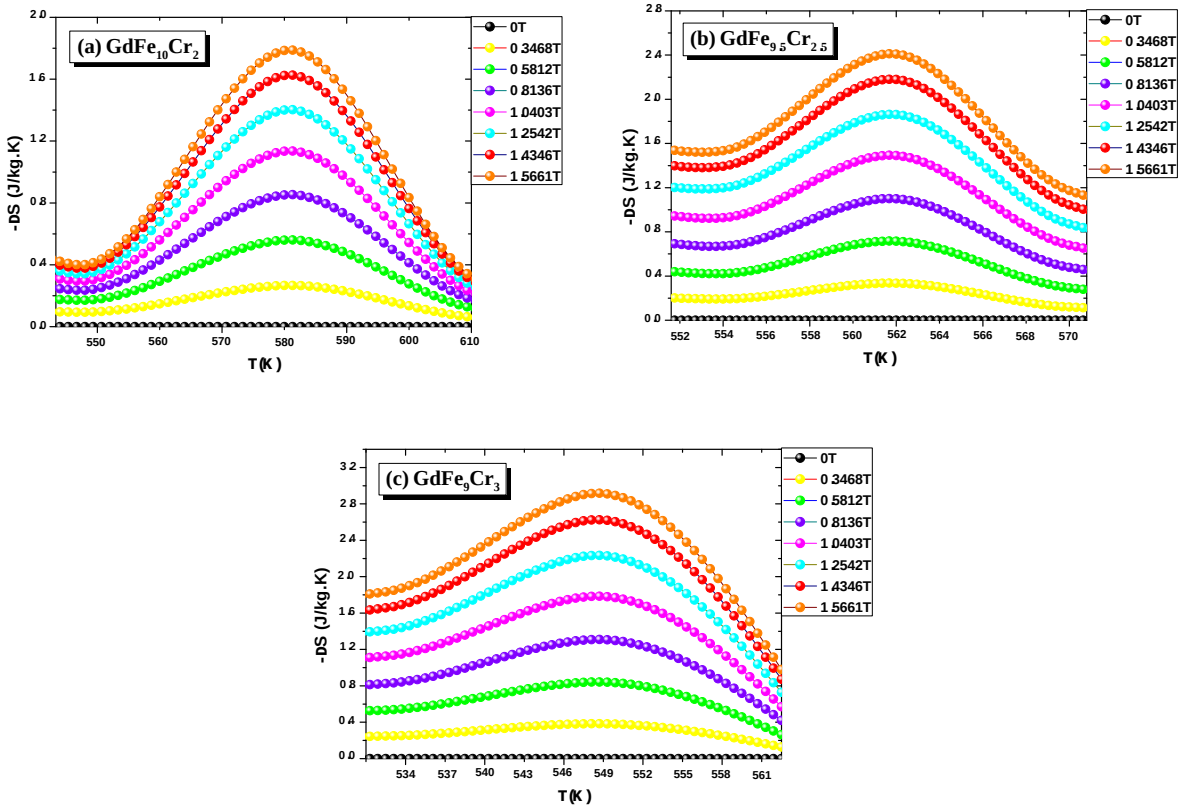

FIG. 15. Entropy change of $GdFe_{12-x}Cr_x$ for (a) $x = 2$, (b) $x = 2.5$ and (c) $x = 3$.

($x = 2$, 2.5 and 3) compounds under a magnetic field of 1.5 T are displayed in Table IX. From this board, we can note that the relative cooling power factor increases significantly with Cr substitution from 12.5 J/kg K to 30.4 J/kg K for $x = 2$ and $x = 3$, respectively. As a result, the studied compounds are strongly suggested for use as active refrigerants for magnetic refrigeration technology.

TABLE IX. Values of T_C, maximum of entropy variation $-\Delta S_{\max}$, and relative cooling power RCP for $GdFe_{12-x}Cr_x$ ($x = 2$, 2.5 and 3) compounds.

Compounds	$GdFe_{10}Cr_2$	$GdFe_{9.5}Cr_{2.5}$	$GdFe_9Cr_3$
T_C (K)	580	562	549
$-\Delta S_{\max}$ (J/kg.K)	1.82	2.44	2.95
RCP (J/kg)	10.5	18.5	28.4

V. CONCLUSION

To sum up, we have studied the structural, magnetic and magnetocaloric properties of $GdFe_{12-x}Cr_x$ (x = 2, 2.5 and 3) samples prepared by arc melting subsequent annealing at 1073 K for one week. Rietveld refinement of the XRD-ray powder diffraction patterns shows that the samples crystallize in the tetragonal $ThMn_{12}$-type structure with $I4/mmm$ space group. The Rietveld analysis indicates that chromium atoms substitute iron in the site $8i$. This result is in good agreement with the Mössbauer study presented in this paper. Thermo-magnetic measurements of the $GdFe_{12-x}Cr_x$ (x = 2, 2.5 and 3) intermetallic compounds show that the ferromagnetic-paramagnetic phase transition temperature (T_C) decreases linearly with increasing Cr content. This reduction of the Curie temperature from 580 K for $GdFe_{10}Cr_2$ to 549 K for $GdFe_9Cr_3$ can be explained by the modification of the exchange interactions due to the substitution of Fe by Cr. The preferential Cr site occupation was demonstrated to be the $8i$ site by means of Rietveld analysis, Mössbauer spectrometry, and first-principle calculations. In addition, we have obtained a good agreement between the results of magnetic moments obtained from calculated hyperfine fields and electronic structure. In order to check the nature of the magnetic phase transition, we have studied the Arrott plots. The positive slopes of the curves indicate that all the samples undergo a second-order magnetic phase transition at T_C. Magnetocaloric effect of the $GdFe_{12-x}Cr_x$ (x = 2, 2.5 and 3) compounds was examined from isothermal magnetization versus magnetic field measured over a wide range of temperatures surrounding Curie temperature. Besides, the magnetic entropy change was determined through the thermodynamic Maxwell relations using the $M(\mu_0 H, T)$ data. $\Delta S_{\max}$ is found to reach 1.82 J/kg K, 2.44 J/kg K, and 2.95 J/kg K for x = 2, 2.5 and 3, respectively. Additionally, the relative cooling power is found to increase greatly, up to 30.4 J/kg for $GdFe_9Cr_3$. The obtained values of the magnetic entropy variation and RCP suggest that our compounds are promising materials for ecologically friendly magnetic refrigeration technology.

VI. ACKNOWLEDGMENTS

This work was mainly supported by the CNRS, ICMPE, France, and the Tunisian Ministry of Higher Education and Scientific Research and Technology (LAB MESLAB), Uni-

versity of Sfax, Tunisia.

---

[1] E. Garces, K. V. Blommestein, J. Anthony, J. H. Eltingand T. Daim, and B. S. Yoon. *Sustainable, Production and Consumption*, 12:221, 2017.

[2] X. Chen, S Omer, M. Worall, and S. Riffat. *Renew. Sust. Energ. Rev.*, 19:629, 2013.

[3] J. R. Gómez, R. F. Garcia, J.C., and M. R. Gómez. *Int. J. Refrigeration*, 36:1388, 2013.

[4] B. F. Yu, Q. Gao, B. Zhang, X. Z. Meng, and Z. Chen. *Int. J. Refrigeration*, 26:622, 2003.

[5] K. A. Gschneidner, V. K. Pecharsky, and A. O. Tsokol. *Rep. Prog. Phys.* , 68:1479, 2005.

[6] M. H. Phan and S. C. Yu. *J. Magn. Magn. Mater.*, 308:325, 2007.

[7] L. W. Li. *Chin. Phys. B.*, 25:037502, 2016.

[8] L. Li, Y. Yuan, Y. Qi, Q. Wang, and S. Zhou. *Mater. Res. Lett.*, 6:67, 2018.

[9] Y. K. Zhang. *J. Alloys Compd.*, 787:1173, 2019.

[10] G. Hadjipanaysis, S. C. Cornelison, J. A. Gerber, and D. J. Sellmyer. *J. Magn. Magn. Mater.*, 21:101, 1980.

[11] D. B. de Mooij and K. H. J. Buschow. *J. Less-Common. Met.*, 136:207, 1988.

[12] R. Coehoorn. *Phys. Rev. B*, 41:11790, 1990.

[13] K. H. J. Buschow. *Rep. Prog. Phys.* , 54:1123, 1991.

[14] K. H. J. Buschow. *J. Magn. Magn. Mater.*, 100:79, 1991.

[15] R. Coehoorn. *J. Magn. Magn. Mater.*, 99:55, 1991.

[16] N. H. Duc, T. D. Hien, P. E. Brommer, and J. J. M. Franse. *J. Magn. Magn. Mater.*, 104:1252, 1992.

[17] R. Reisser, M. Seeger, and H. Kronmüller. *J. Magn. Magn. Mater.*, 128:321, 1993.

[18] X. C. Kou, H. Kronmuller, D. Givord, and M. F. Rossignol. *Phys. Rev. B*, 50:3849, 1994.

[19] L. Bessais, C. Djega-Mariadassou, A. Nandra, M. D. Appay, and E. Burzo. *Phys. Rev. B*, 69:64402, 2004.

[20] L. Bessais, E. Dorolti, and C. Djega-Mariadassou. *Appl. Phys. Lett.*, 87, 2005.

[21] S. Khazzan, N. Mliki, L. Bessais, and C. Djega-Mariadassou. *J. Magn. Magn. Mater.*, 322:224, 2010.

[22] S. Suzuki, T. Kuno, K. Urushibata, K. Kobayashi, N. Sakuma, K. Washio, M. Yano, A. Kato, and A. Manabe. *J. Magn. Magn. Mater.*, 401:259, 2016.

[23] Y. Hirayama, Y.K. Takahashi, S. Hirosawa, and K. Hono. *Scr. Mater.*, 138:62, 2017.

[24] Y. Harashima, T. Fukazawa, and T. Miyak. *Scr. Mater.*, 179:12, 2020.

[25] H. M. Sanchez, D. Salazar, L. E. Zamora, J. S. T. Hernandez, J. A. Tabares, and G. A. P. Alcazar. *Hyperfine Interact.*, 241:44, 2020.

[26] D. Ogawa, T. Yoshioka, X.D. Xu, Y.K. Takahashi, H. Tsuchiura, T. Ohkubo, S. Hirosawa, and K. Hono. *J. Magn. Magn. Mater.*, 497:165965, 2020.

[27] R. Grössinger and R. Sato. *J. Magn. Magn. Mater.*, 294:91, 2005.

[28] L. Zheng, B. Cui, L. Zhao, W. Li, and G. C. Hadjipanayis. *J. Alloys Compd.*, 539:69, 2012.

[29] R. Guetari, R. Bez, C. B. Cizmas, N. Mliki, and L. Bessais. *J. Alloys Compd.*, 579:156, 2013.

[30] R. Guetari, R. Bez, A. Belhadj, K. Zehani, A. Bezergheanu, N. Mliki, L. Bessais, and C. B. Cizmas. *J. Alloys Compd.*, 588:64, 2014.

[31] Z. J. Mo, J. Shen, L. Q. Yan, X. W. Gao, C. C. Tang, J. F. Sun, and B. G. Shen. *J. Alloys Compd.*, 618:512, 2015.

[32] S. Charfeddine, K. Zehani, L. Bessais, and A. Korchef. *J. Solid State Chem.*, 238:15, 2016.

[33] A. Bajorek, K. Prusik, M. Wojtyniak, and G. Chelkowska. *Mater. Chem. Phys.*, 177:299, 2016.

[34] W. Bouzidi, N. Mliki, and L. Bessais. *J. Magn. Magn. Mater.*, 441:566, 2017.

[35] N. Bouchaala, M. Jemmali, T. Bartoli, K. Nouri, I. Hentech, S. Walha, L. Bessais, and A. Ben Salah. *J. Solid State Chem.*, 258:501, 2018.

[36] S. Pakhira, C. Mazumdar, D. Choudhury, R. Ranganathan, and S. Giri. *Phys. Chem. Chem. Phys.*, 20:13580, 2018.

[37] K. Nouri, T. Bartoli, A. Chrobak, J. Moscovici, and L. Bessais. *J. Electron. Mater.*, 47:3836, 2018.

[38] M. Saidi, K. Nouri, S. Walha, E. Dhahri, A. Kabadou, M. Jemmali, and L. Bessais. *J. Electron. Mater.*, 48:2242, 2019.

[39] H. Chen, Y. Yao, F. Yun, J. Qu, Y. Li, Z. Cheng, Z. Ye, S. P Wang, and R. Zheng. *J. Magn. Magn. Mater.*, 498:166099, 2020.

[40] X. Song, X. Zhou, T. Yuan, J. Wang, M. Yue, and T. Ma. *J. Alloys Compd.*, 816:152620, 2020.

[41] D. Givord and R. Lemaire. *IEEE Trans. Magn.*, 10:109, 1974.

[42] C. Piqué, J. A. Blanco, R. Burriel, E. Abad, M. Artigas, and M. T Fernández-Díaz. *Phys. Rev. B*, 75:224424, 2007.

[43] K. H. J. Buschow. *Rep. Prog. Phy.*, 40:1179, 1977.

[44] I. Felner, I. Nowik, and M. She. *J. Magn. Magn. Mater.*, 38:172, 1983.

[45] F. R. De Boer, Y. K. Huang D. B. De Mooij, and K. H. J. Buschow. *J. Less-Common. Met.*, 135:629, 1987.

[46] J. Yang, P. Oleinek, and K. H. Müller. *J. Appl. Phys.*, 88:988, 2000.

[47] L. Bessais, S. Sab, C. Djega-Mariadassou, and J. M. Greneche. *Phys. Rev. B*, 66:054430, 2002.

[48] B. Fuquan, J. L. Wang, O. Tegus, W. Dagula, F. M. Tang, F. M. Yang, G. H. Wu, E. Brück, F. R. De Boer, and K. H. J. Buschow. *J. Magn. Magn. Mater.*, 290:1192, 2005.

[49] S. Khazzan, N. Mliki, and L. Bessais. *J. Appl. Phys.*, 105:103904, 2009.

[50] R. Verhoef, F. R. De Boer, Z. D. Zhang, and K. H. J. Buschow. *J. Magn. Magn. Mater.*, 75:319, 1988.

[51] K. H. J. Buschow. *J. Less-Common. Met.*, 144:65, 1988.

[52] B. P. Hu, H. S. Li, J. P. Gavigan, and J. M. D. Coey. *J. Phys.: Condens. Matter*, 1:755, 1989.

[53] P. Stefanski, A. Kowalczyk, and Wrzeciono. *J. Magn. Magn. Mater.*, 265:70, 1989.

[54] K. Ohashi, Y. Tawara, R. Osugi, and M. Shimao. *J. Appl. Phys.*, 64:5714, 1988.

[55] H. S. Li and J. M. D. Coey. *Handbook of Magnetic Materials*, volume 6. Elsevier, 1991.

[56] K. Kobayashi, S. Suzuki, T. Kuno, K. Urushibata, N. Sakuma, M. Yano, T. Shoji, A. Kato, and A. Manabe. *J. Magn. Magn. Mater.*, 426:273–278, 2017.

[57] Y. Hirayam, Y. K. Takahashi, S. Hirosaw, and Hono. *Scripta Mater.*, 138:62, 2017.

[58] A. M. Gabay and G. C. Hadjipanayis. *Scr. Mater*, 154:284–288, 2018.

[59] G. C. Hadjipanayis, A. M. Gabay, A. M. Schönhöbel, A. Martín-Cid, J. M. Barandiaran, and D. Niarchos. *Engineering*, 6:141, 2020.

[60] M. Saidi, S. Walha, K. Nouri, A. Kabadou, L. Bessais, and M. Jemmali. *J. Alloys Compd.*, 792:87, 2019.

[61] W. Kohn and L. J. Sham. *Phys. Rev.* , 140:A1133, 1965.

[62] P. Hohenberg and W. Kohn. *Phys. Rev.* , 136:B864, 1964.

[63] P. Blaha, K. Schwarz, G. K. H. Madsen, D. Kvasnicka, J. Luitz, R. Laskowski, F. Tran, and L. D. Marks. *WIEN2k, An Augmented Plane Wave + Local Orbitals Program for Calculating Crystal Properties*. Karlheinz Schwarz, Techn. Universitat Wien, Austria, 2018, ISBN: 3-9501031-1-2.

[64] P. Blaha, K. Schwarz, F. Tran, R. Laskowski, G. K. H. Madsen, and L. D. Marks. *J. Chem. Phys.*, 152:074101, 2020.

[65] J. P. Perdew, K. Burke, and M. Ernzerhof. *Phys. Rev. Lett.*, 77:3865, 1996.

[66] K. Schwarz and P. Blaha. *Comput. Mater. Sci.*, 28:259, 2003.

[67] G. Olsson and A. Rosen. *Phys. Rev. A*, 25:658, 1982.

[68] S. Blügel, H. Akai, R. Zeller, and P. H. Dederichs. *Phys. Rev. B*, 35:3271, 987.

[69] H. Rietveld. *Acta Crystallogr.*, 22:151, 1967.

[70] H. Rietveld. *J. Appl. Crystallogr.*, 2:65, 1969.

[71] J. Rodriguez-Carvajal, M. T. Fernandez-Diaz, and J. L. Martinez. *J. Phys.* , 81:210, 2000.

[72] J. Rodriguez-Carvajal. *Physica B* , 192:55, 1993.

[73] L. Bessais, S. Sab, C. Djega-Mariadassou, N. H. Dan, and N. X. Phuc. *Phys. Rev. B*, 70:134401, 2004.

[74] K. Younsi, V. Russier, and L. Bessais. *J. Appl. Phys.*, 107:083916, 2010.

[75] L. Bessais, C. Djega-Mariadassou, D. K. Tung ad V. V. Hong, and N. X. Phuc. *J. Alloys Compd.*, 455(1):35, 2008.

[76] S. Khazzan, L. Bessais, G. Van Tendeloo, and N. Mliki. *J. Magn. Magn. Mater.*, 363:125, 2014.

[77] W. X. Zhong, B. Chevalier, T. Berlureau, J. Etourneau, J. M. D. Coey, and J. M. Cadogan. *J. Less-Common. Met.*, 138:235, 1988.

[78] D. P. Middleton, S. Mishra, G. J. Long, O. A. Pringle, Z. Hu, W. B. Yelon, F. Grandijean, and K. H. J. Buschow. *J. Appl. Phys.*, 78:5568, 1995.

[79] J. J. Bara, B. F. Bogacz, A. T. Pedziwiatr, P. Stefanski, A. Szlaferek, and Wrzeciono. *J. Alloys Compd.*, 265:70, 1998.

[80] Z. Hu, W. B. Yelon, X. Zhang, and W. J. James. *J. Magn. Magn. Mater.*, 79:5522, 1996.

[81] M. Bacmann, C. Baudelet, D. Fruchart, D. Gignoux, E. K. Hlil, G. Krill, M. Morales, R. Verta, and P. Wolfers. *J. Alloys Compd.*, 383:166, 2004.

[82] V. K. Pecharsky and K. A. Gschneidner. *J. Appl. Phys.*, 86:565, 1999.

[83] M. Forker, A. Julius, M. Schulte, and D. Best. *Phys. Rev. B*, 57:11565, 1998.

[84] E. Burzo. *Rep. Prog. Phys.* , 61:1099, 1998.

[85] L. Bessais, C. Djega-Mariadassou, and E. Koch. *J. Phys.: Condens. Matter*, 14:8111, 2002.

[86] L. Bessais and C. Djega-Mariadassou. *Phys. Rev. B*, 63:054412, 2001.

[87] F. M. Yang, Q. Li, , R. Zhao, J. Kuang, F. R. de Boer, J. P. Liu, K. V. Rao, G. Nicolaides, and K. H. J. Buschow. *J. Alloys Compd.*, 177:93, 1991.

[88] L. Néel. *J. Phys. Radium*, 9:148, 1948.

[89] A. Kowakzyk and A. Wrzeciono. *Phys. Stat. Sol. (a)*, 110:241, 1988.

[90] O. Moze and K. H. J. Buschow. *J. Alloys Compd.*, 233:165, 1996.

[91] C. Piquer, F. Grandjean, O Isnard, V. Pop, and G. J. Long. *J. Alloys Compd.*, 377:1, 2004.

[92] L. Ke and D. D. Johnson. *Phys. Rev. B*, 94:024423, 2016.

[93] T. Fukazawa, H. Akai, Y. Harashima, and T. Miyake. *J. Phys. Soc. Jpn*, 87:044706, 2018.

[94] A. M. Schönhöbel, R. Madugundo, A.M. Gabay, J.M. Barandiaran, and G.C. Hadjipanayis. *J. Alloys Compd.*, 2019.

[95] H. Suzuki, A. Nambu, and M. Okamoto. *Phys. Rev. B*, 100:144443, 2019.

[96] J. Trygg, B. Johansson, and M. S. S. Brooks. *J. Magn. Magn. Mater.*, 104:1447, 1992.

[97] X. B. Liu, Z. Altounian, and D. H. Ryan. *J. Alloys Compd.*, 688:118, 2016.

[98] K. Das and I. Das. *J. Appl. Phys.*, 119:093903, 2016.

[99] S. K. Banerjee. *Phys.Lett.*, 16:12, 1964.

[100] A. M. Tishin and Y. I. Spichkin. *The Magnetocaloric Effect and its Applications*. Institute of Physics Publishing, Dordrecht, 2003.

[101] M. Foldeaki, R. Chahine, and T. K. Bose. *J. Appl. Phys.*, 77:3528, 1995.

[102] K. Nouri, M. Jemmali, S. Walha, K. Zehani, A. Ben Salah, and L. Bessais. *J. Alloys Compd.*, 672:440, 2016.

[103] A. V. Morozkin, A. V. Knotko, V. O. Yapaskurt, J. Yao, F. Yuan, Y. Mozharivskyj, R. Nirmala, S. Quezado, and S. K Malik. *J. Solid State Chem.*, 232:150, 2015.

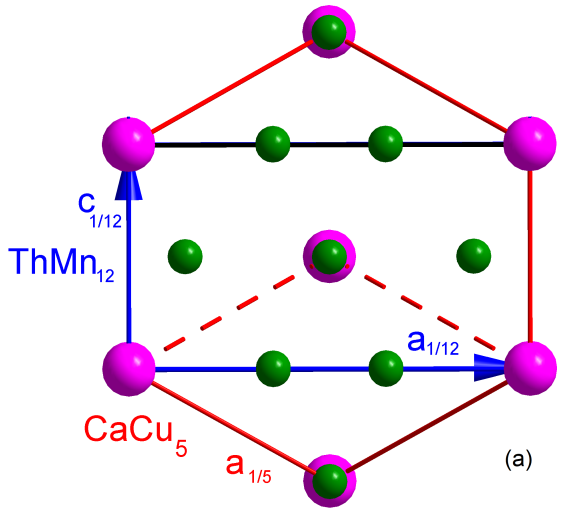
c 1/12
ThMn12
a1/12
CaCu5
a 1/5
(a)

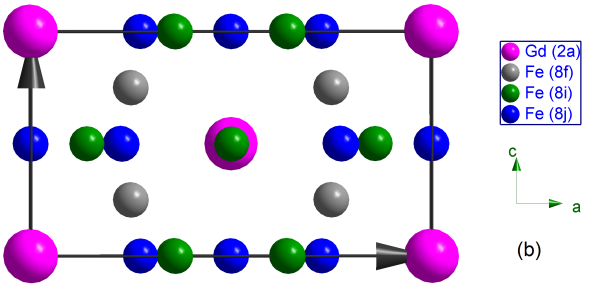
Gd (2a)
Fe (8f)
Fe (8i)
Fe (8j)
c
a
(b)

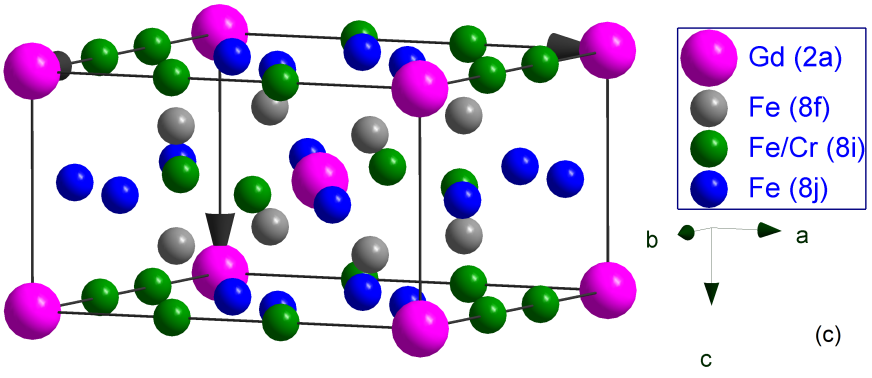
Gd (2a)
Fe (8f)
Fe/Cr (8i)
Fe (8j)
b
a
c
(c)